Real space calculation of optical constants from optical to x-ray frequencies

M. P. Prange,[1] J. J. Rehr,[1] G. Rivas,[2] J. J. Kas,[1] and John W. Lawson[3]
[1]*Department of Physics, University of Washington, Seattle, Washington 98195, USA*
[2]*Instituto de Ingeniería y Tecnología, Universidad Autónoma de Ciudad Juárez, Juárez 32310, Mexico*
[3]*NASA Ames Research Center, Mail Stop 229-1, Moffett Field, California 94035, USA*
(Received 17 October 2008; revised manuscript received 20 July 2009; published 5 October 2009)

We present a theory of linear optical constants based on the single-particle density operator and implemented in an extension of the real space multiple scattering code known as FEFF. This approach avoids the need to compute wave functions explicitly and yields efficient calculations for frequencies ranging from the IR to hard x-rays, which is applicable to arbitrary aperiodic systems. The approach is illustrated with calculations of optical properties and applications for several materials and compared with existing tabulations.

DOI: 10.1103/PhysRevB.80.155110 PACS number(s): 78.20.Bh, 78.70.Dm

I. INTRODUCTION

This work focuses on theoretical calculations of *optical constants*, i.e., the long-wavelength limit $\vec{q}\to 0$ of the dielectric function $\epsilon(\vec{q},\omega)$. These quantities include the complex dielectric constant $\epsilon(\omega)$, the complex index of refraction, the energy-loss function, the photoabsorption coefficient, and the optical reflectivity. Many other important physical properties can be derived from the optical constants such as the photon scattering amplitude per atom, inelastic mean-free paths, and Hamaker constants. However, the *ab initio* calculation of these optical properties for arbitrary materials has been a long-standing problem in condensed-matter physics.[1–5] Thus in practice, these properties are often approximated from atomic calculations or taken from a variety of tabulated compilations.[6–11] However, such tabulations are available only for a small number of well-characterized materials over limited spectral ranges and atomic calculations ignore solid-state effects. Thus we aim to develop an efficient theoretical method covering a broad range of frequencies and applicable to aperiodic materials, thereby providing a practical alternative or complement to tabulated data, atomic models or first principles methods for periodic systems.

The theory of dielectric response has been developed extensively over the past several decades, especially for periodic systems,[1] following pioneering works of Nozières and Pines,[2] Ehrenreich and Cohen,[3] Adler,[4] and Wiser.[5] These authors developed the self-consistent field approach for the dielectric function within the time-dependent Hartree approximation, also known as the random phase approximation (RPA). Subsequently the theory has been extended to include exchange effects within the time-dependent density-functional theory (TDDFT).[12,13] More elaborate theories have been developed that take into account quasiparticle effects and particle-hole interactions based on the Bethe-Salpeter equation (BSE) and Hedin's GW approximation to the electron self-energy.[14–16] Several implementations of GW-BSE (Refs. 17–21) and TDDFT (Refs. 20, 22, and 23) have recently become available. However, computational demands generally restrict these implementations to limited spectral ranges and relatively small or periodic systems.

In an effort to help remedy this situation we have developed an efficient, real space approach within the adiabatic local-density approximation that can be applied to arbitrary condensed systems from the visible to hard x-rays. Our approach is based on a density operator formalism within an effective single-particle (quasiparticle) theory. Here the density operator $\rho(E)=\mathrm{Im}\,G(E)$ is the imaginary part of the one-particle Green's operator $G(E)=(E-H+i\delta)^{-1}$, where (see Appendix) H is the one-particle Hamiltonian including the self-energy and δ is a positive infinitesimal. From $\rho(E)$, both the spectral function $\rho(\vec{r},\vec{r}',E)$ and the local density of states $\rho(\vec{r},E)$ can be obtained. This approach is a generalization of the real space Green's function method implemented in the FEFF codes,[24] which includes both core- and valence-level spectra and builds in inelastic losses and other solid-state effects. Our work is intended to extend the capabilities and ease-of-use of FEFF to enable *full spectrum* output with a quality roughly comparable to that in currently available tabulated data.[6–11] This effort was begun by one of us using an atomic approximation for the initial core and semicore states.[25] That approximation is often adequate at medium high (i.e., soft x-ray) energies, but can be unsatisfactory for optical and UV spectra.

The remainder of this paper is arranged as follows. Section II describes the theoretical formalism behind our approach; Sec. III presents typical results for various optical constants for a number of materials; Sec. IV discusses some additional applications and diagnostics, and Sec. V presents a brief summary and conclusions.

II. THEORY

A. Real space theory of dielectric response

We consider the macroscopic linear response of extended systems to an external electromagnetic field of polarization $\hat{\epsilon}$ and frequency ω

$$V_{\mathrm{ext}}(t)=V_{\mathrm{ext}}(\omega)e^{\delta t-i\omega t}+cc, \tag{1}$$

where δ is a positive infinitesimal corresponding to adiabatic turn on of the perturbing potential. Throughout this work we use Hartree atomic units ($\hbar=m=e^2=a_0=1$), unless otherwise specified. This perturbation polarizes the material, inducing a steady-state change $\delta n(\vec{r},\omega)e^{-i\omega t}+cc$ in the microscopic electron density, which leads to a macroscopic polarization $\vec{P}(\omega)e^{-i\omega t}+cc$, representing the average *screening* dipole re-

sponse of the electrons to the applied field. For simplicity, we assume that $\vec{P}$ has no component perpendicular to the applied electric field. This is the case for systems of cubic or higher symmetry in the $q \to 0$ limit, but relaxing this restriction poses no computational difficulty. In this case one can define a scalar electric susceptibility χ, in terms of which the dielectric function is[26]

$$\epsilon(\omega) = 1 + 4\pi\chi(\omega),$$

$$\vec{P} = \chi\vec{D}. \tag{2}$$

Here $\vec{D} = -\vec{\nabla}V_{\text{ext}}$ is the external electric field. Also here and elsewhere in this paper, the dielectric function is represented in dimensionless, relative units where the dielectric constant of the vacuum $\epsilon_0 = 1$. Our calculations here make use of an effective single-particle microscopic theory in which the N-electron state of the system at time t is described by a Slater determinant of time-dependent single-particle orbitals $\phi_i(t)$. This state can be characterized by the time-dependent single-particle density matrix $\rho(t)$ which is the projector onto the subspace defined by the occupied orbitals $\phi_i(t)$,

$$\rho(t) = \sum_{i=1}^{N} |\phi_i(t)\rangle\langle\phi_i(t)|. \tag{3}$$

The time evolution of these orbitals is governed by the time-dependent Schrodinger equation

$$i\frac{d}{dt}|\phi_i(t)\rangle = H|\phi_i(t)\rangle, \tag{4}$$

where H is taken to be the time-dependent Kohn-Sham such as Hamiltonian including self-energy corrections

$$H = -\frac{1}{2}\nabla^2 + V_{\text{nuc}} + V_H + V_{\text{xc}} + \Sigma_d + V_{\text{ext}}(t). \tag{5}$$

The terms in Eq. (5) are, respectively, the kinetic energy, the electrostatic attraction to the nuclei V_{nuc}, the Hartree potential V_H, the ground-state exchange-correlation potential V_{xc}, the dynamical contribution to the quasiparticle self-energy correction in the GW plasmon-pole approximation Σ_d (i.e., the full self-energy is $\Sigma = V_{\text{xc}} + \Sigma_d$), and the time-dependent external potential $V_{\text{ext}}(t)$ of Eq. (1). Thus this Hamiltonian is non-Hermitian and includes final state damping. Here and below, we suppress the position dependence of quantities when no confusion will result. The time evolution in Eq. (4) implies the Liouville equation[3] for the density matrix

$$i\frac{d\rho}{dt} = H\rho - \rho H^{\dagger}. \tag{6}$$

In order to obtain the optical constants, we first linearize this equation with respect to the ground-state by decomposing the Hamiltonian and density matrix into their values in the ground state and contributions induced by $V_{\text{ext}}(t)$

$$H = H_0 + H_1(t) = H_0 + V_{\text{ext}}(t) + V_{\text{ind}}(t)$$

$$\rho = \rho_0 + \rho_1. \tag{7}$$

The time-dependent perturbation $H_1(t)$ consists of the external field plus a term V_{ind} due to the response of the electrons. Second order terms, i.e., the products $\rho_1 H_1$ and $H_1\rho_1$ are discarded. We assume, as appropriate for linear response, that the induced potential $V_{\text{ind}}(t)$ and hence $H_1(t)$ *have the same time dependence as* $V_{\text{ext}}(t)$. With these assumptions, the time derivative in Eq. (6) becomes trivial and we can formally solve for the induced density matrix in terms of the stationary Kohn-Sham (KS) orbitals $|\phi_i^0\rangle$ and eigenvalues E_i of the ground-state system,

$$\rho_1(\omega) = \sum_{i,j} (f_i - f_j)\frac{|\phi_i^0\rangle\langle\phi_i^0|H_1|\phi_j^0\rangle\langle\phi_j^0|}{\omega - (E_j - E_i) + i\delta}, \tag{8}$$

where $f_i = f(E_i) \approx \theta(\mu - E_i)$ is the Fermi occupation number of state $|\phi_i^0\rangle$ and μ is the Fermi level. The KS orbitals obey the unperturbed Schrodinger equation

$$i\frac{d}{dt}|\phi_i^0(t)\rangle = H_0|\phi_i^0(t)\rangle. \tag{9}$$

The Fourier components of the induced electron density $\delta n(\vec{r},\omega)$ due to the perturbation V_{ext} is then given by

$$\delta n(\vec{r},\omega) = \langle\vec{r}|\rho_1(\omega)|\vec{r}\rangle. \tag{10}$$

At this point it is convenient to introduce the bare and full susceptibilities whose local behavior is given by

$$\delta n(\vec{r},\omega) = \langle\vec{r}|\chi^0(\omega)H_1|\vec{r}\rangle = \langle\vec{r}|\chi(\omega)V_{\text{ext}}|\vec{r}\rangle. \tag{11}$$

Typically, the bare response χ^0 to an external perturbation is first computed from a single-particle (i.e., noninteracting) description of the ground state. The full response χ of the system can be related to response χ^0 of the noninteracting reference system. This procedure gives rise to the Dyson equation for χ with an interaction kernel K

$$\chi = \chi^0 + \chi^0 K\chi = \chi^0(1 - K\chi^0)^{-1}. \tag{12}$$

Methods for computing optical response that start from a single-particle description of the ground state can be classified by their approximations to the particle-hole interaction kernel K. The accuracy of the calculated macroscopic properties reflects that of the noninteracting response and the interaction kernel. Note, for example, that one needs to find the frequency-dependent response of the noninteracting system, which involves different considerations than those for static, ground-state properties such as the total energy and density.

In the crudest approximation $K = 0$, the resulting polarizability is that of the noninteracting reference system and local fields are also neglected. For this case there is no screening and the single-particle potential is the sum of the ground-state potential and V^{ext}. An obvious deficiency of the noninteracting response is that the Coulomb field of the induced density is neglected. To correct this deficiency, Adler[4] and Wiser[5] independently developed equivalent theories of the macroscopic dielectric response of periodic solids based on the RPA, where K is taken to be the bare Coulomb interaction. These theories were originally built on band-structure calculations for periodic materials in the Hartree approxima-

tion, and Hartree local fields were included through the now termed *Adler-Wiser formula*. In this approach the operator inversion of Eq. (12) is reformulated using the inverse of the microscopic dielectric matrix $\epsilon_{GG'}(\omega,\vec{k})$, which is then spatially averaged to give the macroscopic response $\epsilon(\omega) = \lim_{k\to 0} 1/[\epsilon^{-1}(\vec{k},\omega)]_{0,0}$. However, the Adler-Wiser dielectric function is that of the Hartree system and has the deficiency that the underlying electronic wave function is not antisymmetric under particle interchange.

Going beyond the RPA requires additional exchange-correlation effects in K. There have been efforts along these lines of two types: those based on TDDFT and those based on many body perturbation theory and the BSE. These approaches have been critically compared by Onida *et al.*[1] By considering excited states from a quasiparticle viewpoint,[16] the interaction kernel can be decomposed into a direct term K^D, which is the Coulomb interaction between the quasiparticles and an exchange interaction K^X,

$$K = K^X + K^D. \tag{13}$$

Expanding Eq. (12) in singly-excited particle-hole (i.e., one electron, one hole) states, and taking $K^D \equiv W = \epsilon^{-1} v$ to be the Coulomb interaction screened by an effective (microscopic) dielectric function, yields a set of approximations referred to as the BSE. Various screening models have been used in W ranging from parametrized models (e.g., the Levine-Louie dielectric function) to the independent-particle approximations such as the static RPA. Currently BSE schemes are computationally demanding, since the inverse in Eq. (12) involves a product basis which is typically very large. The differences between the independent-particle excitation energies and optical spectra and their interacting counterparts which build in particle-hole interactions are referred to as excitonic effects. On the other hand, the use of density-functional theory permits a great simplification in which the nonlocality of the exchange-correlation terms is avoided by lumping the exchange-correlation effects in K^D into a local functional $f_{\mathrm{xc}}[\rho(\vec{r})]$. Then the approach reduces to the TDDFT approximation (Ref. 12) where

$$K(\omega) = v + f_{\mathrm{xc}}(\omega), \quad f_{\mathrm{xc}}(\omega) = \frac{\delta V_{\mathrm{xc}}}{\delta \rho}. \tag{14}$$

Consequently a local approximation to $V_{\mathrm{xc}}[\rho]$ leads to a local kernel, in which K depends only on the diagonal elements of the real space single-particle density operator. This locality implies that Eq. (12) can be expanded in a single-particle basis, thus circumventing the need for particle-hole states as in the BSE. The cost of this simplification is that detailed information concerning the particle-hole interaction (e.g., exciton wave functions) is only implicit. Nevertheless, calculations in such TDLDA frameworks are now in wide use.[27,28] While the TDDFT gives good agreement with experiment for optical spectra in many cases, quantitative agreement at higher energies has been more elusive. Due to computational demands, calculations with the BSE tend be even more limited. Moreover, these wave-function based methods were originally designed for static or relatively low excitation energies, and become cumbersome due to the need for large basis sets and special exchange-correlation functionals to describe excited states at high energies.

The above difficulties have led us to consider a different approach with the goal of developing a general method for calculations of optical response that can handle a variety of systems and spectral range. Our approach is based on an extension of real space multiple scattering theory (RSMS) in terms of the one-particle density operator. The RSMS approach is well suited to treat arbitrary aperiodic condensed-matter systems over a very broad frequency range, from the visible to hard x-rays. Indeed, this scattering-theoretic approach provides a superior basis for very high energy (i.e., x-ray) spectra, where scattering is weak and the approach converges rapidly. Furthermore the approach goes beyond the Born-Oppenheimer approximation in that the approach can include some effects of nuclear motion in terms of correlated Debye-Waller factors.[29]

In this work, we present calculations within this RSMS approach using an independent quasiparticle approximation for the single particle states. Comparing Eqs. (10) and (11) gives an expression for the bare response function or susceptibility in terms of the orbitals ϕ_i^0

$$\chi^0(\vec{r},\vec{r}',\omega) = \sum_{i,j} (f_i - f_j) \frac{\phi_i^0(\vec{r})\phi_i^{0\dagger}(\vec{r}')\phi_j^0(\vec{r}')\phi_j^{0\dagger}(\vec{r})}{\omega - (E_j - E_i) + i\delta}. \tag{15}$$

Formally the imaginary part of the dielectric function is related to the full susceptibility by[12]

$$\epsilon_2(\omega) = \frac{4\pi}{V} \mathrm{Im} \int d\vec{r} d\vec{r}' \ \mathrm{Tr}\, d\chi(\vec{r},\vec{r}',\omega) d^\dagger, \tag{16}$$

where V is the volume of the system, $d = \vec{\alpha}\cdot\vec{\epsilon}_p e^{i\vec{k}\vec{r}}$ is the transition operator between the incident photon of wave-vector $\vec{k}$ and polarization ϵ_p, and Tr refers to a trace over the spinor indices. In practice the transition operator is replaced by the truncation to rank one of its expansion in tensors developed by Grant,[30] which is equivalent to the dipole approximation. To evaluate Eq. (16) for both optical and x-ray energies, we must first compute the bare response function $\chi^0(\vec{r},\vec{r}',\omega)$.

Equation (15) can be expressed without reference to the KS orbitals ϕ_i^0 in terms of the single-particle Green's function $G(E)$ and the density operator $\rho(E) = (-1/\pi)\mathrm{Im}\, G(E)$ as

$$\chi^0(\vec{r},\vec{r}',\omega) = \int^{E_F} \rho(\vec{r},\vec{r}',E) G^+(\vec{r},\vec{r}',E+\omega) + \rho(\vec{r}',\vec{r},E) G^-(\vec{r}',\vec{r},E-\omega) dE. \tag{17}$$

Using the symmetries $\rho(\vec{r},\vec{r}',E) = \rho(\vec{r}',\vec{r},E)$ and $G^-(\vec{r},\vec{r}',E) = [G^+(\vec{r}',\vec{r},E)]^*$ on the real E axis, we can express the results entirely in terms of the spectral functions $\rho(\vec{r},\vec{r}',E)$

$$-\frac{\mathrm{Im}\,\chi^0}{\pi} = \int_{E_F-\omega}^{E_F} \rho(\vec{r}',\vec{r},E)\rho(\vec{r}',\vec{r},E+\omega) dE. \tag{18}$$

In this work we calculate these spectral functions for energies ranging from the lowest occupied states to x-ray ener-

gies of order 100 KeV using the real space Green's functions in FEFF.[24]

B. Multiple scattering Green's function

Our calculations of χ^0 are based on an independent-particle model in which each electron moves in an effective quasiparticle scattering potential $V(\vec{r})$ which implicitly includes a complex dynamic self-energy correction $\Sigma_d(E)$ to the ground-state exchange and correlation potential, i.e., $V_{\rm xc} \rightarrow V_{\rm xc}+\Sigma_d(E)-\Sigma_d(E_F)$. In this work our default $V_{\rm xc}$ is the exchange-correlation potential of von Barth and Hedin and $\Sigma_d(E)$ is calculated using the local *GW* plasmon-pole model of Hedin and Lundqvist.[31] However, more elaborate self-energy approximations can optionally be considered.[32] The potential $V(\vec{r})=\Sigma_n v_n(r_n)+V_0$ is taken to be the self-consistent muffin-tin potential for a cluster of atoms at fixed locations $\vec{R}_n$. Here $\vec{r}_n=\vec{r}-\vec{R}_n$ is the electron position relative to the $n^{\rm th}$ atom, and V_0 is a constant interstitial potential. Note that since the self-energy is complex valued, the Hamiltonian is non-Hermitian and hence the phase shifts are also complex valued, effects which lead to final state self-energy shifts and broadening of the spectra. Within RSMS theory, the Green's function for this potential can be written as a double angular momentum expansion

$$G(\vec{r},\vec{r}',E) = -2k\Bigg[\sum_{LL'} R_{Ln}(\vec{r}_n)\tilde{G}_{Ln,L'n'}\bar{R}_{L'n'}(\vec{r}'_{n'}) + \delta_{n,n'}\sum_{L} H_{Ln}(\vec{r}_>)\bar{R}_{Ln'}\vec{r}_<\Bigg], \quad (19)$$

where n and n' are the sites nearest $\vec{r}$ and $\vec{r}'$, respectively, and $\vec{r}_>$ ($\vec{r}_<$) is the larger (smaller) of the two position vectors. The terms in Eq. (19) are the right-hand-side regular and irregular solutions R_{Ln}, H_{Ln} of the spherically symmetric single-site problems and their left-side counterparts $\bar{R}_{Ln}$, $\bar{H}_{Ln}$ the partial-wave phase shifts δ_{ln}, and the multiple scattering (MS) matrix $\tilde{G}_{Ln,L'n'}$ defined by Eq. (A16). The wave functions are normalized so that in the interstitial region R_{Ln} coincides with $Y_L[h_l^+e^{i\delta_{ln}}-h_l^-e^{-i\delta_{ln}}]/2i$, and H_{Ln} coincides with $Y_L h_l^+ e^{i\delta_{ln}}$. The bar for the left-sided solutions indicates that all factors except the Bessel functions are complex conjugated. Equation (19) is rederived in the Appendix. As detailed there, all these ingredients except for the MS matrix can be found from the solution of a spherically symmetric single-particle quantum mechanics problem. The full MS matrix G for the system is found by numerical matrix inversion (e.g., with the LU or Lanczos algorithms in FEFF) with typical matrix dimensions of order 2×10^3, or by using the MS path expansion.

C. Relativistic basis

In order to include relativistic effects such as spin-orbit coupling in our calculations properly, it is necessary to recast the Green's function in terms of spinor solutions to the Dirac equation. In this context it is convenient to expand the spin-angular dependence of the one-electron states in the Pauli spinor-valued spin-orbit eigenfunctions which diagonalize both total and orbital angular momentum

$$\chi_K(\hat{r}) = \sum_{\sigma=-1/2}^{1/2} Y_l^{m_j-\sigma}(\hat{r})\phi^\sigma\left\langle l,\frac{1}{2},m_j-\sigma,\sigma|j,m_j\right\rangle. \quad (20)$$

Here ϕ^σ is a Pauli spinor, $K=(\kappa,m_j)$ is a pair of relativistic angular momentum quantum numbers and $\langle l,s,m_l,m_s|j,m_j\rangle$ is a Clebsh-Gordan coefficient. In this work as in Refs. 33 and 34, we have constructed the scattering matrix $G_{Ln,L'n'}$ of Eq. (19) using the scattering matrices t_l calculated for the total angular-momentum channel $j=l+1/2$. This matrix is then transformed to the basis of spin-orbit eigenfunctions using Clebsch-Gordan coefficients. The central-site contribution Eq. (A17) is constructed directly from numerical solutions of the central-site problem giving a total relativistic Green's function

$$G(\vec{r},\vec{r}',E) = -2k\Bigg[\sum_{KK'} H_{Kn}(\vec{r}_>)\bar{R}_{K'n'}(\vec{r}_<)\delta_{KK'}\delta_{nn'} + R_{Kn}(\vec{r}_n)\tilde{G}_{Kn,K'n'}\bar{R}_{K'n'}(\vec{r}'_n)\Bigg], \quad (21)$$

written in terms of right-hand (no bars) and left-hand (bars) solutions of the Dirac equation at energy E. These functions are four spinors which can be written in terms of the spin-orbit eigenfunctions:

$$R_{Kn}(\vec{r}_n) = \frac{1}{r_n}\begin{pmatrix} P_\kappa(r_n)\chi_\kappa^{m_j}(\hat{r}_n) \\ iQ_\kappa(r_n)\chi_{-\kappa}^{m_j}(\hat{r}_n)\end{pmatrix}$$

$$\bar{R}_{Kn}(\vec{r}_n) = \frac{1}{r_n}\begin{pmatrix} P_\kappa(r_n)\chi_\kappa^{m_j\dagger}(\hat{r}_n) \\ -iQ_\kappa(r_n)\chi_{-\kappa}^{m_j\dagger}(\hat{r}_n)\end{pmatrix}^T, \quad (22)$$

where the T in Eq. (22) denotes the transposed vector. The irregular solutions H, $\bar{H}$ take a similar form. These solutions are normalized by requiring the upper-component radial wave functions to coincide with $[h_l^+e^{i\delta_{\kappa n}}-h_l^-e^{-i\delta_{\kappa n}}]/2i$ (regular solution) or $h_l^+e^{i\delta_{\kappa n}}$ (irregular solution) beyond the muffin-tin radius. Here we are using the notation of Grant,[30] to which the reader is referred for details regarding the numerical solutions P, Q appearing in Eq. (22). Tamura[35] gives a relevant and illuminating discussion of solutions to the Dirac equation in spherical coordinates, although he treats a more general case using different notation. We have also transformed to a basis of real spherical harmonics to simplify calculations of the real-valued spectral functions in the presence of a complex-valued self-energy.

D. Complex scattering potential

The construction of the self-consistent muffin-tin scattering potential for the one-particle states is described elsewhere,[36] and we only briefly summarize the process here. First, a Dirac-Fock solver is used to calculate free-atomic potentials and densities, which are then overlapped to obtain a starting point for the self-consistency loop. In this loop the one-particle Green's function for the full multiple scattering problem is calculated, from which a new electron density is

calculated. Finally a ground-state muffin-tin potential is constructed based on the calculated density within the local density approximation (LDA) of density functional theory (DFT). The loop is iterated to self-consistency which typically takes about 10–20 iterations. Self-energy corrections are subsequently added for unoccupied states within the GW plasmon-pole approximation.

E. Core response

At low energies (below the bottom of the valence band), the density operator becomes discrete in energy, taking nonzero values only at isolated eigenvalues. In this regime, it is more computationally efficient to use local atomic orbitals to describe the core-electronic structure. Thus, we separate the single-particle density operator into two energy regions: the core region in which the atomic approximation is valid to high accuracy and the solid-state region where solid-state effects are important,

$$\rho(E) = \begin{cases} \rho^{\text{core}}(E) & E < E_{\text{cv}}, \\ \rho^{\text{val}}(E) & E > E_{\text{cv}}. \end{cases} \tag{23}$$

The core-valence separation energy E_{cv} is chosen to be away from all KS eigenvalues that separates the two regimes, and is set by default to -40 eV; this value is typically about 30 eV below the Fermi level. Above this energy $\rho(E)$ is derived from the single-particle Green's function as described below. Note that in general there are occupied and unoccupied states above E_{cv}, but there are no unoccupied states below E_{cv}. Similarly, the dielectric function $\epsilon_2(\omega)$ can be separated into contributions $\epsilon_2^{\text{core}}(\omega)$ and $\epsilon_2^{\text{val}}(\omega)$ arising from transitions with core and valence initial states, respectively.

As noted above, the deep core states are represented by single-particle atomiclike orbitals ϕ_ν, which are described accurately by Dirac-Fock atomic states for a single atomic configuration.[37] Here the index $\nu=(n,i)$ denotes both a site index n and atomic level index i for the particular bound state at that site (e.g., $1s, 2s$, $2p_{1/2}$, etc.). Thus we replace $\rho(E)$ in Eq. (18) for $E<E_{\text{cv}}$ with

$$\rho_{\text{core}}(E) = \sum_\nu \rho_{\text{at}}^{(\nu)}(E),$$

$$\rho_{\text{at}}^{(\nu)}(E) = \phi_\nu(\vec{r})\phi_\nu(\vec{r}')\delta(E-\epsilon_\nu). \tag{24}$$

We thereby recover an expression equivalent to Fermi's golden rule for the core contribution to the dielectric response

$$\epsilon_2^{\text{core}}(\omega) = \sum_\nu \epsilon_2^\nu(\omega)$$

$$= \frac{4\pi}{\omega}\sum_\nu \text{Im}\langle\nu|\hat{d}^\dagger\hat{G}(\omega+\epsilon_\nu)\hat{d}|\nu\rangle\theta(\omega+\epsilon_\nu-\epsilon_F). \tag{25}$$

For energies below $E_{\text{cv}} \approx \mu - 30$ eV $< V_0$ the eigenfunctions of the central-site problem are tightly bound to the central atom; their wave functions decay rapidly as a function of the distance from the central site and can be taken to vanish in all cells except the central cell. This, along with the selection rules, limits the elements $G_{Kn,K'n'}$ (representing the final states) that contribute to absorption. For core initial states, the final state energy includes the inverse core-hole lifetime Γ_ν which broadens ϵ^ν. The calculation of the density operator matrix elements appearing in Eq. (16) is handled differently depending on the photoelectron energy $E=\omega+\epsilon_\nu$. For low-energy (less than ≈ 50 eV$+V_0$) the final state Green function $G(\omega)$ is calculated by a full multiple scattering (FMS) , as in the calculation of ϵ_2^{val}. At very high energies where the fine structure is negligible, we can again employ an atomic model and neglect scattering contributions [i.e., $G_{Kn,K'n'}=0$ in Eq. (21)]. At intermediate energies (50 eV$+V_0 \le E \le 1000$ eV) we use efficient path filters[38] developed to treat extended x-ray-absorption fine structure to find the dominant terms in the multiple scattering path expansion and sum these contributions to obtain the necessary $G_{Kn,K'n'}$ elements,

$$G = G^0 + G^0TG^0 + \ldots . \tag{26}$$

The calculation of ϵ_2^{core} is accomplished by looping over the edges ν with eigenvalues below E_{cv}. For each edge we calculate ϵ_2^ν via either FMS, path expansion, or the atomic approximation on appropriate energy grids. At this stage, correlated Debye-Waller factors can be included, as in conventional x-ray absorption spectroscopy (XAS) calculations with routines in FEFF.

F. Valence response

For real energies, the spectral function can be expressed entirely in terms of the regular solutions R_{Kn} and the irregular solutions do not contribute. Using the formal relation between the density operator and the one-particle Green's function $\rho(E)=(-1/\pi)\text{Im}\, G(E)$ and the fact that $\text{Im}\, H_\kappa = R_\kappa$ one obtains from Eq. (21) the spectral function

$$\rho^{\text{val}}(\vec{r},\vec{r}',E) = \sum_{K,K'} R_{Kn}(\vec{r})\hat{\rho}_{Kn,K'n'}R_{K'n'}(\vec{r}'_{n'}), \tag{27}$$

with

$$\hat{\rho}_{Kn,K'n'} = \delta_{n,n'}\delta_{K,K'} + \text{Im}(i^l\tilde{G}_{Kn,K'n'}i^{l'}) \tag{28}$$

which is valid for $\vec{r}$ in cell n and $\vec{r}'$ in cell n', where $R_{Kn}(\vec{r})=\chi_K(\hat{r}_n)R_{\kappa n}(r_n)$. Below the Fermi level on the real energy axis, the density operator is a rapidly varying function of energy. Away from the real axis, however, the variation with energy is much smoother. To retain both the separable form of Eq. (27) and the smoothness of $G(\omega)$ away from the real axis, we introduce a small broadening Γ and renormalize the regular solutions, so that the central atom spectral function gives virtually the same local density of states (DOS) in each Norman sphere as the broadened spectral function:

$$\tilde{R}_{\kappa n}(r;E) = A_{\kappa n}(E,\Gamma)\text{Re}[R_{\kappa n}(r;E+i\Gamma)],$$

$$\int_0^{r_n^N} [\tilde{R}_{\kappa n}(r;E)]^2 r^2 dr = \mathrm{Im} \int_0^{r_n^N} r^2 dr R_{\kappa n}(r;E+i\Gamma) H_{\kappa n}(r;E+i\Gamma). \quad (29)$$

This approximation is a key simplification in our approach. Here the Norman radius r_n^N is defined as the radius of a neutral sphere centered on the n^{th} atom of the charge distribution formed by overlapping the charge distributions of the isolated atoms in their solid-state positions. The separable representation of the real space density operator in Eq. (27) permits a separation of the double spatial integral in Eq. (16) into a product of two one-dimensional integrals. To complete the spatial integral in Eq. (16), we make the approximation that the spherical Norman cells n partition space and define the full integrals over space as summations of integrals over individual cells

$$\int d\vec{r} \to \sum_n \int_{\vec{r}\in n} d\vec{r} = \sum_n \int_0^{r_N^{(n)}} r_n^2 dr_n \int d\Omega_n. \quad (30)$$

The dipole matrix elements at each site n are defined in terms of the renormalized (right- and left-handed) regular solutions:

$$M^n_{K,K'}(E,E') = \int_{\vec{r}\in n} d\vec{r} \tilde{R}_{Kn}(\vec{r};E) d\tilde{\tilde{R}}_{K'n}(\vec{r};E'). \quad (31)$$

In the dipole approximation the matrix elements vanish except for transitions with $j' = j \pm 1$. Left (right) circularly polarized light only induces transitions with $m_j' = m_j + 1 (m_j' = m_j - 1)$. Thus the transition matrix M is sparse. Relaxing the dipole approximation is straightforward. Doing so introduces additional nonzero elements to M. With these conventions, the contribution to the spectrum from the response of the valence states (i.e., those occupied single-particle states with eigenvalues above E_{cv}) is given entirely in terms of spectral functions and dipole matrix elements,

$$\epsilon_2^{\text{val}}(\omega) = \frac{4\pi}{V} \int_{E_F-\omega}^{E_F} dE \sum_{n,n'} \rho_{nn'}(E) M_{n'}(E,E+\omega) \times \rho_{n'n}(E+\omega) M_n^T(E+\omega,E), \quad (32)$$

where $\rho_{nn'}$ and M_n are matrices in a truncated relativistic angular momentum $K=(\kappa,\mu)$ space. By symmetry, the sum over sites n in Eq. (32) can be reduced to a sum over inequivalent sites in the material. To compute ϵ_2^{val} we first solve the Dirac equation at each inequivalent site which yields T. Then $G_{LnL'n'}$ is found by inverting the full multiple scattering matrix, and matrix elements M are evaluated using the wave functions from the calculation of T. Finally, Eq. (32) is evaluated using trapezoid rule integration for the energy integrals.

G. Spectrum construction

With the response of both the valence band and the more tightly bound electrons calculated, the contribution from each core edge is then interpolated onto a final output grid and combined with the other core edges and with the valence contribution, yielding

$$\epsilon_2(\omega) = \sum_\nu \epsilon_2^{(\nu)}(\omega) + \epsilon_2^{\text{val}}(\omega). \quad (33)$$

III. THEORETICAL OPTICAL CONSTANTS

We now illustrate our approach with a number of examples for each of several optical constants. The examples presented here are for the most part monatomic crystals (metals and insulators) with a single inequivalent site. However, the generalization to heterogeneous materials is straightforward, and an example is also presented for Al_2O_3. Aperiodic materials can be treated as well by including enough sites in a cluster to converge the spectrum. All of these materials have well-characterized structures and experimental data have been compiled over a broad range.[6,10,39,40] For example, the data in Ref. 10 were obtained by combining existing experimental data using a Kramers-Kronig analysis with measurements at the Deutsches Elektronen-Synchrotron light source that improve the composite data around 40 eV. While these tabulations do not explicitly give error bars, one can roughly assess the uncertainties by comparing the different data sources. Since one of the main purposes of this paper is to extend the RSMS approach to relatively low energies, we present a number of comparisons which focus on the low-energy regime. Because of space limitations, the results presented here represent only a small fraction our results. Tabulations of the data presented here and additional comparisons are available on the world wide web (WWW).[41]

A. Computational details

The calculations presented in this section used FMS matrices truncated at $l=3$ and 147 atoms for all materials except diamond. The diamond calculation used $l=2$ and 450 atoms. We have included diamond because it is a difficult case for the real space method due to short, strong covalent bonding. In contrast typical k-space calculations of diamond (such as the plane-wave psuedopotential calculation discussed below)[21] use a unit cell containing only two atoms and are less computationally demanding. All spectra were obtained by summing the contributions from 70 atom clusters. The response for the valence bands is obtained by calculating ρ^{val} on a regular energy grid of 200 points. Then the dipole matrix elements $M(E,E')$ are calculated for all pairs (E,E') with E below the Fermi level and E' above it. Equation (32) is then evaluated by matrix multiplication and simple numerical integration. To compute $\epsilon_2^{\text{val}}(\omega)$ to high frequencies, we employ an atomic model of the valence bands based on average band energies and occupations calculated from ρ^{val}. The core-state response is first calculated on a set of five 100 point frequency grids for each core initial state κ in the embedded-atom approximation. The FMS and path-expansion calculations are then carried out in cluster sizes of around 175 atoms on frequency grids of approximately 120

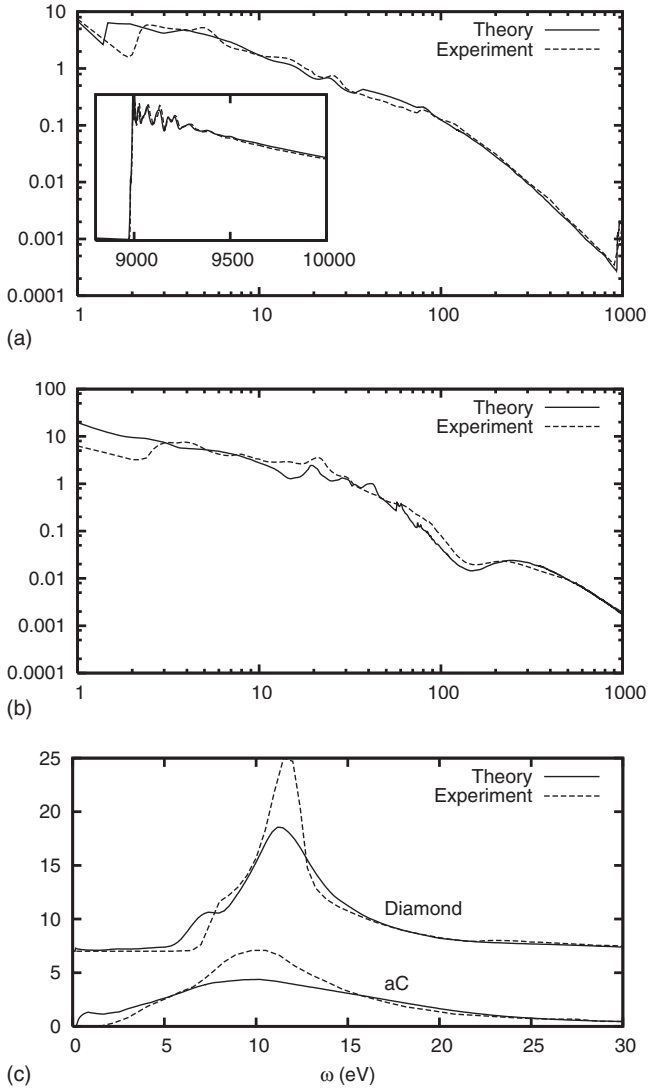

FIG. 1. Calculated and experimental (Refs. 10 and 44) values of ϵ_2 (dimensionless) for Cu (a), Au (Ref. 10) (b), and C diamond (Ref. 6) and amorphous (Ref. 45) (c). In the bottom panel the diamond curves have been shifted vertically for clarity.

points. The contribution to ϵ_2 for each core initial state and the valence bands are then interpolated onto a large (5×10^5 points) frequency grid which spans the full spectrum (e.g., 10^{-3} through 10^6 eV) and serves as the final output grid. This grid has a higher density of points at low frequencies and around each core edge.

B. Dielectric function: imaginary part

The fundamental physical quantity needed in our calculations of optical response is the imaginary part of the dielectric function $\epsilon_2(\omega)$, which is given by Eq. (33). All other optical constants can be obtained in terms of $\epsilon_2(\omega)$ using analytic relations, as described below. Illustrative examples our approach for the calculation of $\epsilon_2(\omega)$ for Cu and Au are plotted in Fig. 1 and compared to experiment. Also, in order to demonstrate the effects of structural disorder on the dielectric response, we compare the imaginary part of the dielectric function for diamond and amorphous Carbon in Fig. 1. Amorphous carbon structures were obtained with a "melt-and-quench" algorithm[42] using first principles molecular dynamics as implemented in the VASP package.[43] These results, as well as those presented below and calculations for other materials, are currently available in both graphical and tabular form on the FEFF website.[41]

C. Dielectric function: real part

Owing to the analyticity of the dielectric response, the real and imaginary parts of the dielectric function are related by the Kramers-Kronig relation[26]

$$\epsilon(\omega) = 1 + \frac{2}{\pi}\mathcal{P}\int_0^\infty d\omega' \frac{\omega' \epsilon_2(\omega')}{\omega^2 - \omega'^2}. \tag{34}$$

Here $\mathcal{P}$ indicates the principal value of the integral. Since the integrand in Eq. (34) has a pole at $\omega' = \omega$ care must be taken when evaluating the transform numerically. Then to evaluate the integral in Eq. (34) over the interval $[\omega_i, \omega_{i+1})$ between the i^{th} and $(i+1)^{\text{th}}$ grid points we find a linear approximation $\epsilon_2(\omega') = m\omega' + b$. This linearization allows us to rewrite the Kramers-Kronig transform as

$$\mathcal{P}\int_{\omega_i}^{\omega_{i+1}} d\omega' \frac{\omega' \epsilon_2(\omega')}{\omega^2 - \omega'^2} = m(\omega_i - \omega_{i+1}) + \frac{m\omega - b}{2}\ln\left(\frac{\omega_{i+1} + \omega}{\omega_i + \omega}\right) - \frac{m\omega + b}{2}\ln\left|\frac{\omega_{i+1} - \omega}{\omega_i - \omega}\right|. \tag{35}$$

This expression is used to produce ϵ_1 on a grid consisting of the midpoints of the intervals of the grid upon which ϵ_2 has been calculated. Linear interpolation is then used to construct both real and imaginary parts of the dielectric function on the original grid. This procedure ensures that the arguments of the logarithms in Eq. (36) are finite and positive.

The results of this procedure for diamond, Cu, and Al_2O_3 are plotted in Fig. 2. The numerical transform Eq. (36) is stable and accurate and (along with the calculated ϵ_2) completely determines ϵ_1 via Eq. (34). Nevertheless, we find that the real part of the dielectric function is more sensitive to errors and approximations than the imaginary part.

D. Energy loss

With both real and imaginary parts of $\epsilon(\omega)$ one can easily obtain the energy-loss function

$$-\text{Im}\,\epsilon^{-1}(\omega) = \frac{\epsilon_2(\omega)}{\epsilon_2^2(\omega) + \epsilon_1^2(\omega)}. \tag{36}$$

This is illustrated for Cu, Al_2O_3, and Au in Fig. 3. The loss function is proportional to the long-wavelength limit of the dynamic structure factor $S(\vec{q}, \omega)$, which can be measured by inelastic scattering of either electrons in electron-energy-loss spectroscopy (EELS) or photons in nonresonant inelastic x-ray scattering. Calculations of the latter performed in a real space multiple scattering framework analogous to ours at finite momentum transfer $\vec{q}$.[46] However, these calculations are restricted to core electrons response. As for ϵ_2, we find that

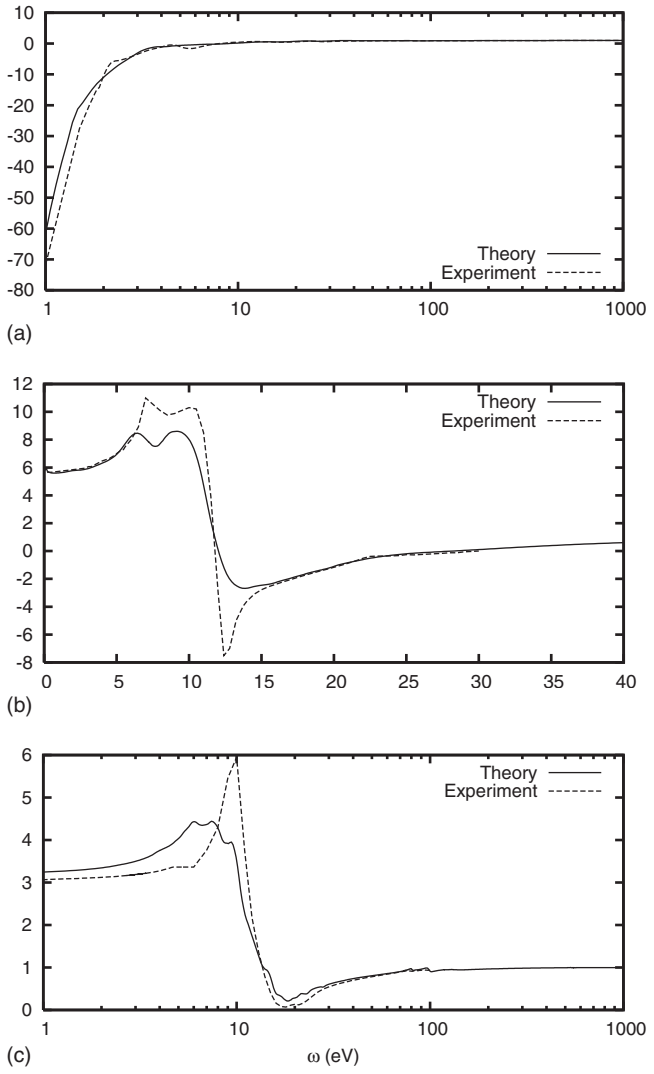

FIG. 2. Calculated ϵ_1 (dimensionless) for Cu (a) and C (diamond) (b), and Al_2O_3 (c) compared to tabulated experiment. (Refs. 6 and 10)

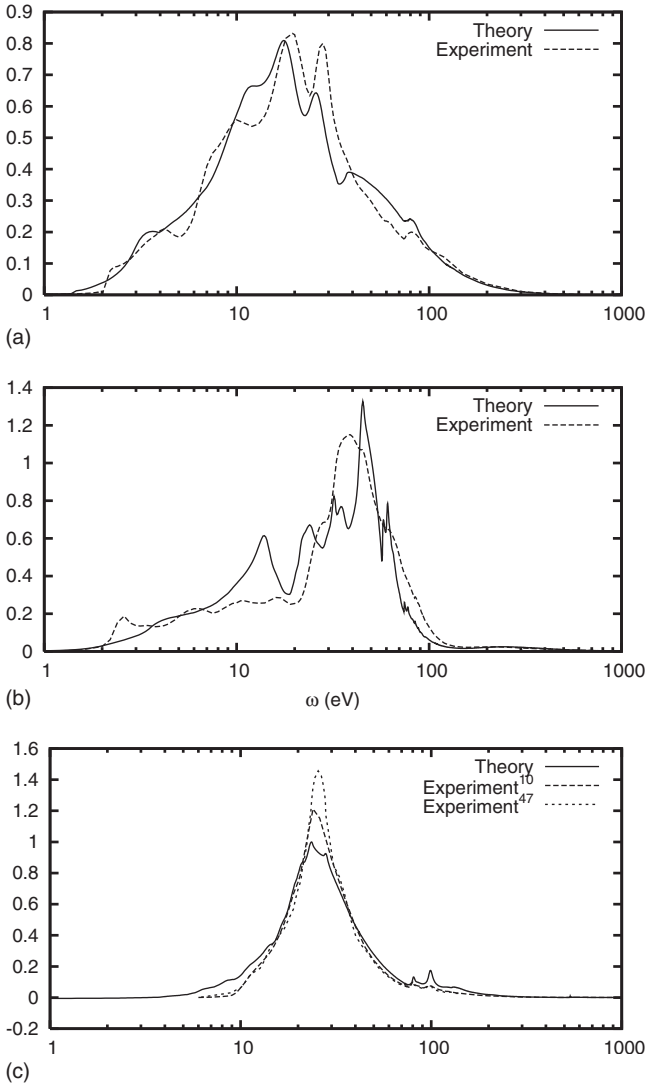

FIG. 3. Calculated energy-loss function (dimensionless, from Eq. (36)) for Cu (a), Au (b), and Al_2O_3 (c) compared to experiment. (Refs. 10 and 47) The Al_2O_3 result is compared to both x-ray (Ref. 10) and EELS (Ref. 47) experiments.

the loss function is *less* sensitive to errors and approximations in the density operator than ϵ_1. In a discussion of the differences between absorption and EELS, Onida, *et al.*[1] have given an explanation of this observation in terms of the long-range part of the Coulomb interaction.

E. Index of refraction

The complex index of refraction is simply the square root of the complex dielectric function, from which the real and imaginary parts $n(\omega)$ and $\kappa(\omega)$ can be extracted:

$$n(\omega) + i\kappa(\omega) \equiv \epsilon(\omega)^{1/2}. \tag{37}$$

Typical results for the real part of the index of refraction are given in Fig. 4.

F. Absorption coefficient

The photon absorption coefficient $\mu(\omega)$ is defined as the (natural) logarithm of the ratio of the incident and transmitted intensities for a photon beam across a thin sample divided by the thickness. Theoretically $\mu(\omega)$ can be expressed in terms of the imaginary part of the index of refraction $\kappa(\omega)$

$$\mu(\omega) = 2\frac{\omega}{c}\kappa(\omega). \tag{38}$$

Thus, $\mu(\omega)$ is directly measurable with optical absorption experiments in transmission. Such experiments are currently performed to high accuracy using synchrotron light sources. In Fig. 5 we compare our calculated results with experiment for several materials and with a calculation based on electronic structure calculated with ABINIT using the AI2NBSE package,[21] which employs a BSE solver developed at NIST to generate optical spectra. For comparison purposes the AI2NBSE calculations *excludes* both local fields and excitonic effects and was generated using a regular grid of $8^3 = 512$ k points to sample the Brillouin zone, 50 bands, and an

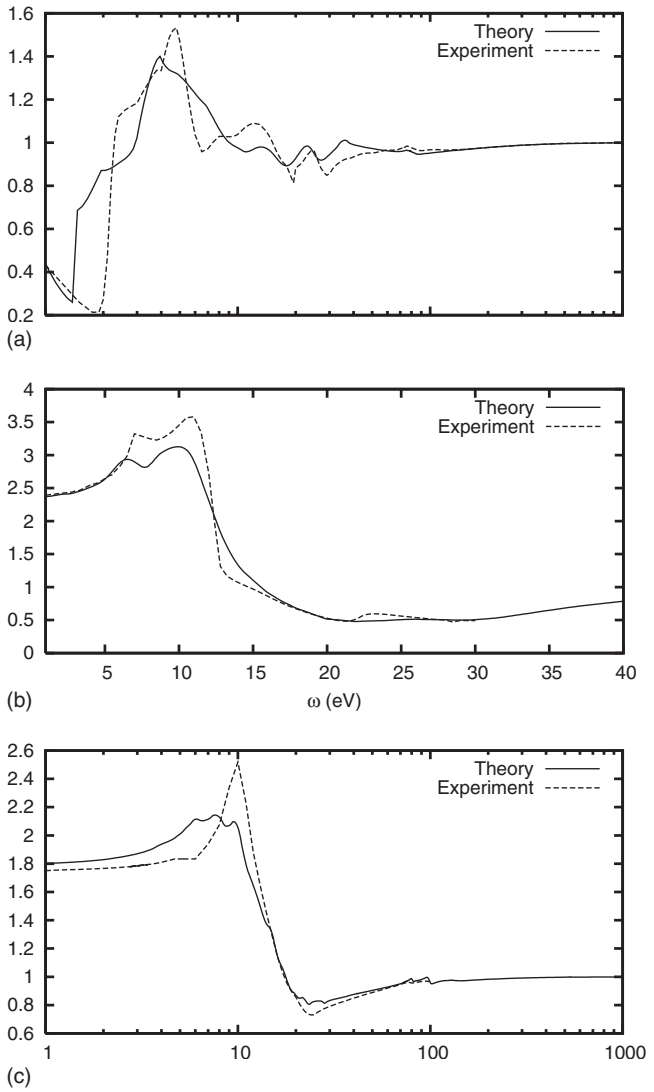

FIG. 4. Calculated real index of refraction for Cu (a), C (diamond) (b) and Al_2O_3 (c), compared to experiment. (Refs. 6 and 10)

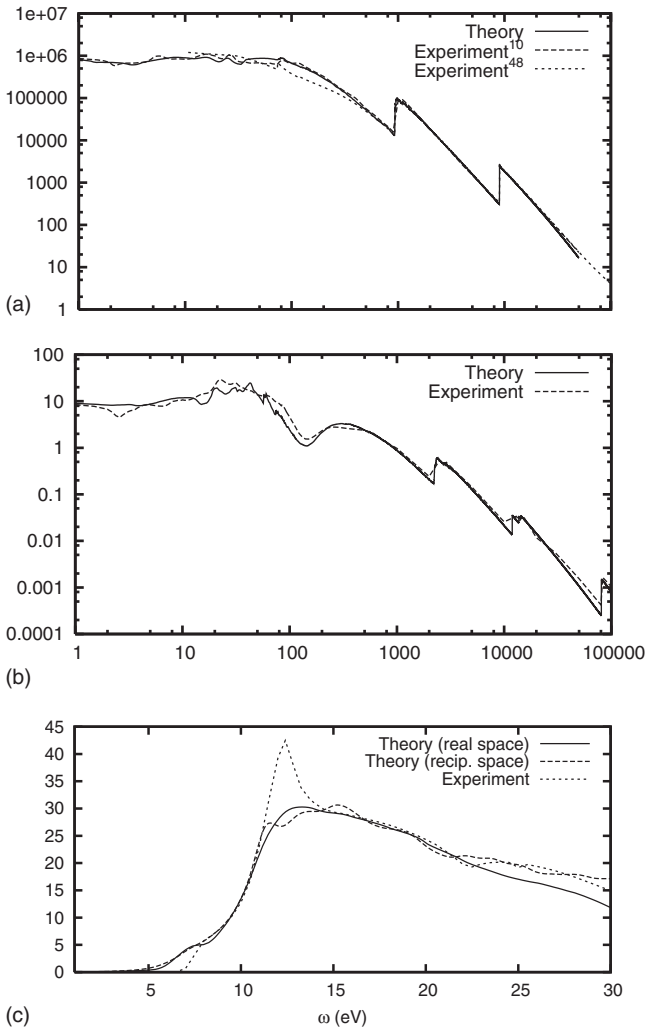

FIG. 5. Calculated absorption coefficient μ in cm^{-1} for Cu (a), Au (b), and C (diamond) (c) compared to experiment. (Refs. 6 and 10) The calculated results for diamond and Cu are compared to reciprocal-space (Ref. 21) and atomic (Ref. 48) calculations, respectively.

energy cutoff of 30 Hartree for the plane-wave basis. The C 1*s* electrons were treated with a Troullier-Martins psuedopotential. For comparison purposes, no gap corrections were included in either calculation.

G. Reflectivity

An important optical experiment for materials that can be prepared by vapor deposition methods is the measurement of the normal incidence reflectivity $R(\omega)$ defined as the ratio of the power reflected from a planar face of a sample to the incident power. This quantity can be related to the dielectric response of the material by considering the boundary conditions satisfied by Maxwell's equations at the interface between the sample and vacuum. This procedure produces the familiar Fresnel equations[26] relating the amplitudes of the transmitted (refracted) and reflected waves to the amplitude of the incident wave. As discussed by Stratton,[49] R can be found from the Fresnel equations. For example, for normal incidence

$$R(\omega) = \frac{[n(\omega)-1]^2 + \kappa^2(\omega)}{[n(\omega)+1]^2 + \kappa^2(\omega)}. \tag{39}$$

The general expression for a lossy material[49] ($\epsilon_2 \neq 0$) and arbitrary angle of incidence is complicated. However, we note that away from normal incidence, $R(\omega)$ has polarization dependence even for isotropic media.

H. Photon-scattering amplitude

The Rayleigh forward scattering amplitude $f(\omega)$ for photons can also be computed from the dielectric function[34]

$$f(\omega) = \frac{\omega}{4\pi r_0 c^2}\frac{V}{N}[\epsilon(\omega)-1]. \tag{40}$$

where $r_0 = e^2/mc^2$ is the classical radius of the electron. Consequently, it is straightforward to calculate the x-ray scattering factors including anomalous terms, including solid-state corrections using our RSMS approach, i.e., $f(\vec{q},\omega) = g(q,\omega)$

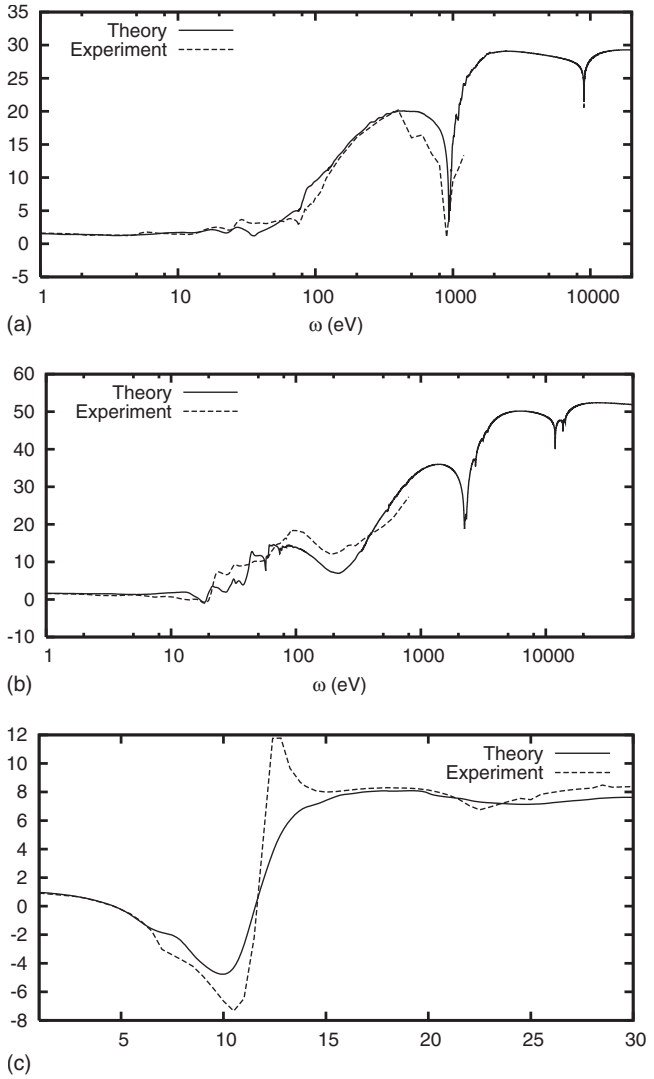

FIG. 6. Calculated real part of the anomalous atomic scattering factor in units of r_0, for Cu (a), and Au (b), and C diamond (c), compared to experiment. (Refs. 6, 10, and 50)

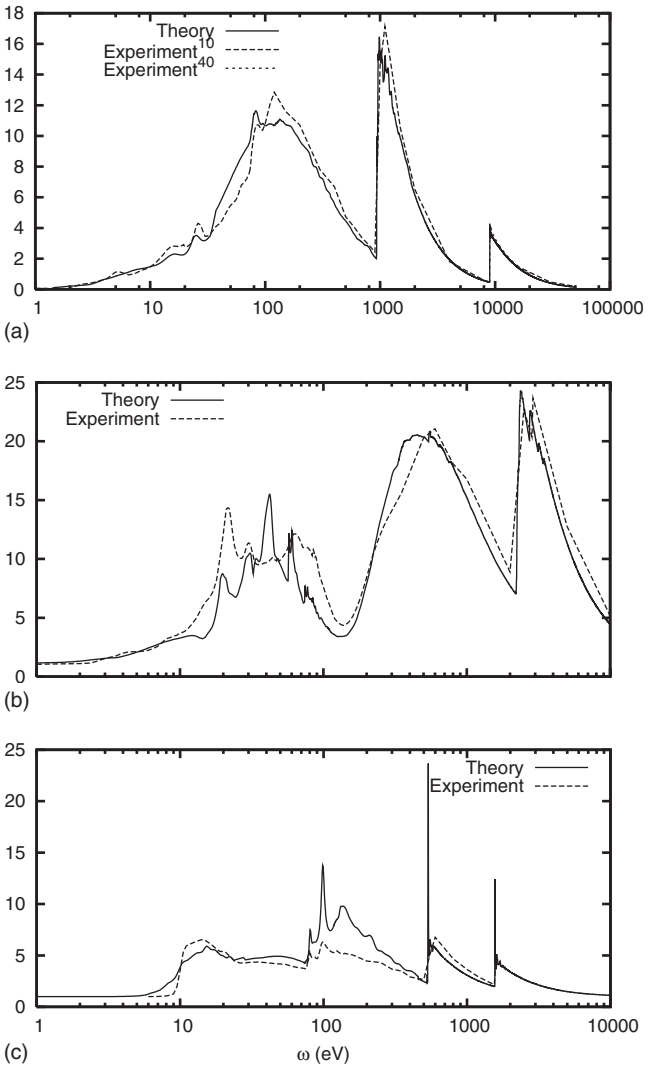

FIG. 7. Calculated imaginary part of the atomic scattering factor in units of r_0 for Cu (a), Au (b), and Al_2O_3 (c) compared to experiment. (Ref. 10 and 40)

$+f^{ss}(\vec{q},\omega)+f_1(\omega)+if_2(\omega)$ in terms of f. Typical calculations of the real and imaginary parts of $f(\omega)$ are illustrated in Figs. 6 and 7.

IV. APPLICATIONS AND DIAGNOSTICS

Optical constants are valuable in a host of applications, of which only a few are illustrated below.

A. Hamaker constant

The Hamaker constant is the (real) function $\epsilon(i\omega)$ obtained from the dielectric function at pure imaginary frequencies and is useful in theoretical calculations of van der Waals coefficients. For example, for separation distances beyond the tunneling regime, the interaction between the tip and sample in an atomic force microscopy experiment is dominated by the van der Waals force, which can be calculated given the tip-sample geometry using the Hamaker constants of the tip and sample.[51] Using the analyticity of ϵ in the upper half plane, the Hamaker constant can be calculated using a Kramers-Kronig type transform as in Eq. (34)

$$\epsilon(i\omega) = 1 + \frac{2}{\pi}\int_0^\infty d\omega' \frac{\omega' \epsilon_2(\omega')}{\omega^2 + \omega'^2}. \tag{41}$$

Likewise we have evaluated Eq. (41) using the same Kramers-Kronig routines. Examples are given on the WWW.[41]

B. Electron self-energies

The energy-loss function $-(1/\pi)\mathrm{Im}\,\epsilon(E)$ is the central ingredient in the many-pole self-energy model,[32] which a generalization of the Hedin-Lundqvist plasmon-pole model based on the GW approximation $\Sigma = iGW$, where G is the Green's function and $W = \epsilon^{-1}V$ is the screened coulomb interaction which is obtained from a many-pole representation of the loss function. This model has been used[32] to improve on

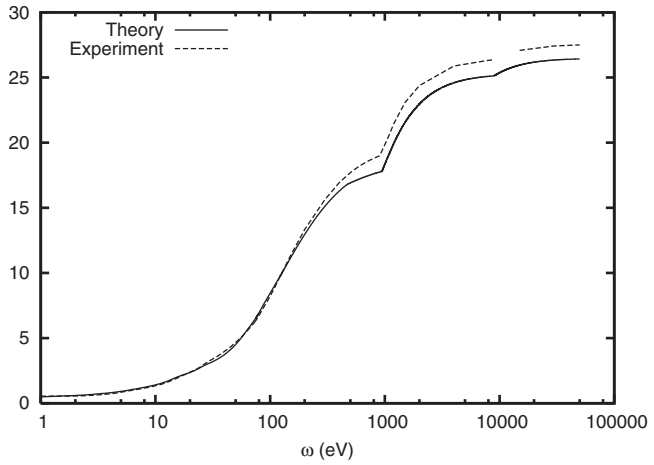

FIG. 8. $n_{\mathrm{eff}}(\omega)$ calculated from the ϵ_2 sum rule for Cu using Eq. (43), which assumes an asymptotic value of 29, the atomic number of Cu, in the $\omega \to \infty$ limit.

the plasmon-pole approximation in XAS calculations using FEFF.

C. Inelastic mean-free paths and stopping powers

The inelastic mean-free path $\lambda(E)$ is directly related to the imaginary part of the self-energy, i.e.,

$$\lambda(E) = \frac{k}{|\Sigma(E)|}, \tag{42}$$

where k is the electron wave number.[52] The optical constants have also be used to calculate electron collision stopping powers, e.g., using a theoretical optical data model.[52] Examples are given on the WWW.[41]

D. Sum rules

We have also included in the output of our codes a few quantities that are useful for internal numerical checks and for understanding the relationship between the underlying electronic structure and the frequency dependence of the optical constants. Thus the f sum rules for the imaginary parts of the dielectric function and the inverse dielectric function provide an important quantitative check of the calculation. The effective number of electrons per atom participating in transitions at frequency ω can be defined as

$$n_{\mathrm{eff}}(\omega) = \frac{V}{2\pi^2 N}\int_0^{\omega} d\omega' \omega' \epsilon_2(\omega'), \tag{43}$$

which has the limit[53]

$$\lim_{\omega\to\infty} n_{\mathrm{eff}}(\omega) = Z, \tag{44}$$

where Z is the number of electrons in the subsystem (e.g., atomic cell) whose number density is N/V in atomic units. The theory and calculations presented here are valid over a frequency range large enough to quantitatively evaluate the limit Eq. (44) as illustrated in Fig. 8. Missing or extra oscillator strength suggests errors in the calculation or possibly a lack of convergence. Another check is given by the index of refraction sumrule

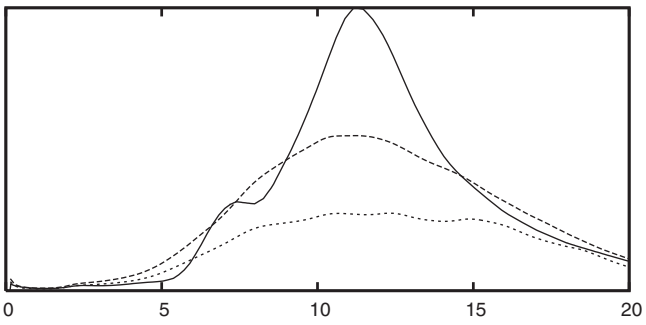

FIG. 9. JDOS$/\omega^2$ (arbitrary units) for $p \to d$ (dashed line) and $p \to s$ (dots) transitions and for comparison the calculated ϵ_2 of this work (solid line) for diamond vs photon frequency in eV.

$$\int_0^{\infty} [n(\omega) - 1] d\omega = 0. \tag{45}$$

E. Joint density of states

As noted above, the selection rules constrain the angular momentum of final and initial states that can contribute to the absorption of light to a few dominant channels (e.g., $p \to d$, $s \to p$, etc.). The joint density of states (JDOS) corresponding to a certain dipole allowed channel ($l \to l'$) is therefore defined in terms of the normal angular momentum projected lDOS ρ_l:

$$\int_{E_f-\omega}^{E_f} \rho_l(E)\rho_{l'}(E+\omega)dE, \tag{46}$$

where the lDOS is given in terms of the density operator by

$$\rho_l(E,r) = \sum_m \int d\vec{r} |Y_L(\hat{r})|^2 \rho(\vec{r},\vec{r},E). \tag{47}$$

Neglecting energy dependence of the dipole matrix elements in the calculation of ϵ_2 gives a spectrum which is a sum of terms proportional to the JDOS$/\omega^2$ for the dipole allowed channels. We show this quantity for transitions from initial states with p character compared to the calculated ϵ_2 for diamond in Fig. 9.

V. CONCLUSIONS

We have developed an efficient approach for semiquantitative *ab initio* calculations of optical constants over a broad spectrum, from the optical to x-ray energies. Our method, based on the one-particle density operator, is implemented in an extension of the RSGF approach in the FEFF codes which does not rely on symmetry and can be applied to aperiodic and nanoscale materials. Thus the approach provides a useful complement to tabulated optical data. We have illustrated the method here for a number of materials for which optical data are also available including metals, insulators, and aperiodic solids. Overall our results for the optical constants are only

semiquantitative in the optical-UV range, but become much more accurate for core-level response at x-ray energies. Also their imaginary parts tend to be more accurate than the real parts. This degree of accuracy is already adequate for many purposes, and especially for theoretical model calculations which are not particularly sensitive to the detailed fine structure in the spectra. These include the calculation of screened Coulomb potentials and van der Waals interactions. Furthermore many improvements are possible: (i) it is desirable to include local-field corrections as described above; (ii) the muffin-tin approximation should be replaced with more accurate *full potentials* in each cell; (iii) the extension to arbitrary momentum transfer $\vec{q}$ is often desirable. As noted above, the calculations can be done for any momentum transfer with only a modest increase in computational effort within our density operator formulation. In fact, the response of core states has already been extended to finite q by Soininen, *et al.*;[46] (iv) for crystalline systems, it may be desirable and sensible to calculate the MS matrix in k space, i.e., with periodic boundary conditions; and (v) the treatment of the particle-hole interaction K currently only takes intraatomic screening into account.

ACKNOWLEDGMENTS

We wish to thank A. Ankudinov, J. Chelikosky, H. Lawler, Z. Levine, S. Louie, L. Reining, E. Shirley, J. A. Soininen, and F. Vila for many discussions and especially G. Hug and M. Jaouen for suggestions during the early stages of this work. This work was supported in part the U.S. Department of Energy, Office of Basic Energy Sciences grant No. DE-FG02-97ER45623 and was facilitated by the DOE CMSN.

APPENDIX: REAL SPACE MULTIPLE SCATTERING GREEN'S FUNCTION

In this Appendix we describe the real space Green's functions used in this work. Formally the Greens function operator is given by

$$G^+(E) = [E - H + i\delta]^{-1}, \tag{A1}$$

where δ is a positive infinitesimal and H is the one-particle Hamiltonian, which in this work is calculated using Eq. (5). Expanding G^+ in the scattering potentials and free propagators G^0 yields the MS expansion

$$G = G^0 + G^0VG = G^0 + G^0TG^0 + \cdots = [1 - \bar{G}^0T]^{-1}G^0. \tag{A2}$$

Here we have presented the local t matrix $t_n = v_n + v_nG^0t$ to sum implicitly over all scatterings at a given site n, where $\langle\vec{r}|t_n|\vec{r}'\rangle = t_n(\vec{r},\vec{r}',E)$ vanishes outside a given cell n where $v(r_n)=0$.

1. Free propagator

In position space the free propagator $G^0(E)$ is given by the FT,

$$G^0(\vec{r},\vec{r}',E) = \int \frac{d^3k}{(2\pi)^3}\frac{e^{i\vec{k}\cdot(\vec{r}-\vec{r}')}}{E - k^2/2 + i\delta}. \tag{A3}$$

Below we evaluate this expression in terms of site angular-momentum scattering states $|L,R\rangle$ which diagonalize t_i

$$j_L(\vec{r}_R) = \langle\vec{r}|L,R\rangle = i^l j_l(kr_R)Y_L(\hat{r}_R)$$

$$\bar{j}_L(\vec{r}_R) = \langle L,R|\vec{r}\rangle = i^{-l} j_l(kr_R)Y_L^*(\hat{r}_R), \tag{A4}$$

where $k = \sqrt{2(E-V_0)}$.

In terms of spherical Bessel functions the free propagator is given everywhere by

$$G^0(\vec{r},\vec{r}',E) = -2k\sum_L Y_L(\hat{r})g_l(r,r')Y_L^*(\hat{r}') \tag{A5}$$

$$= -2k\sum_L h_L^+(\vec{r}_>)\bar{j}_L(\vec{r}_<), \tag{A6}$$

where $g_l(r,r') = h_l^+(kr_>)j_l(kr_<)$ and $h_L^+(\vec{r}) = i^l h_l^+(kr)Y_L(\hat{r})$. This result can be obtained, e.g., by Fourier transformation using the identity $\exp(i\vec{k}\cdot\vec{r}) = 4\pi\Sigma_L j_L(\vec{r})Y_L^*(\hat{k})$ and carrying out the radial integrals in the complex k plane. Alternatively, the same result follows from the inhomogeneous radial differential equation, where the prefactor is obtained from the Wronskian $2/r^2W(j_l,h_l^+) = -2k$. Here, as in the treatment of Rehr and Albers,[54] we have used the phase and normalization conventions of Messiah, with $j_l = (h_l^+ - h_l^-)/2i$ and $i^l h_l(x) = e^{ix}c_l(1/ix)/x$, c_l is a polynomial of degree l with $c_l(0)=1$. Also, for convenience, we have included the phase factors i^l and i^{-l} in h_L^+ and $\bar{j}_L$, respectively, which do not change G^0, but simplify the asymptotic behavior.

The expansion of the free propagator for points at different sites has the form of a matrix product

$$G^0(\vec{r},\vec{r}',E) = \sum_{L,L'} j_L(\vec{r}_R)G^0_{LR,L'R'}\bar{j}_L(\vec{r}_{R'}) = \sum_{L,L'}\langle\vec{r}|LR\rangle\langle LR|G^0(E)|L'R'\rangle\langle L'R'|\vec{r}'\rangle. \tag{A7}$$

This follows directly from Eq. (A6) and the translation formulas for the spherical Hankel functions[54]

$$h_{L'}^+(\vec{r}_R') = \sum_L j_L(\vec{r}_R)G^0_{LR,L'R'}. \tag{A8}$$

Note the implicit factors of $i^{l'}$ and i^l in $j_L(\vec{r}_R)$ and $\bar{j}_{L'}(\vec{r}_R)$ in this representation. In some works, e.g., that of Faulkner and Stocks,[55] these phase factors are included in the definition the propagator matrix elements. The above expression can be checked, e.g., by comparing $i^l h_l^+(kr) = \Sigma_{L'} j_l'(kr_R)i^{l'}G^{0+}_{L'R,L0}$. Equation (A7) can be derived, e.g., by expanding the exponential product $e^{i\vec{k}\cdot(\vec{r}-\vec{r}')} = e^{i\vec{k}\cdot(\vec{r}-\vec{R})}e^{-i\vec{k}\cdot(\vec{r}'-\vec{R}')}e^{i\vec{k}\cdot(\vec{R}-\vec{R}')}$ in spherical Bessel functions, and then carrying out the integration over k. This procedure yields for the dimensionless propagator matrix elements:

$$\tilde{G}^0_{LR,L'R'} \equiv \frac{G^0_{LR,L'R'}}{-2k} = 4\pi \sum_{L''} \langle Y_L Y_{L''} | Y_{L'} \rangle h^+_{L''}(k\vec{R}''), \tag{A9}$$

which depend explicitly on $k\vec{R}''=k(\vec{R}-\vec{R}')$. The FEFF code uses dimensionless matrix elements $\tilde{G}^0_{L,L'}(k\vec{R})$ which have a separable representation[54]

$$\tilde{G}^0_{L,L'}(k\vec{R}) \equiv \tilde{G}^0_{LR,L'R'} = \frac{e^{ikR}}{kR} \sum_{\lambda} \tilde{\Gamma}_{L\lambda} \Gamma_{\lambda,L'}, \tag{A10}$$

$$\rightarrow 4\pi \frac{e^{ikR}}{kR} c_l c_l' Y^*_L(\hat{R}) Y_{L'}(\hat{R}), \quad (kR \rightarrow \infty), \tag{A11}$$

where $\Gamma_{\lambda,L}(k\vec{R})$ are generalized spherical harmonics. This can be obtained, for example, by substituting the asymptotic form of $i^l h_l$ and the completeness relation $\Sigma_L Y^*_L(\hat{k}) Y_L(\hat{R}) = \delta(\hat{k}-\hat{R})$.

2. Full propagator

Let us now evaluate the behavior of the full propagator $G(\vec{r},\vec{r}',E)$ for $\vec{r}$ and $\vec{r}'$ in different cells n and n' respectively. For this case the MS series can be viewed as a sequence of scattering events consisting of all scatterings at site n followed by all sequences of scatterings not scattering at site n first or site n' last, followed by all scatterings at site n',

$$G_{nn'} = [1 + G^0 t_n] \bar{G}_{nn'} [1 + t_{n'} G^0], \tag{A12}$$

where the notation $G_{nn'}$ refers to the propagator starting and ending in cells n and n' respectively, while $\bar{G}_{nn'}$ refers to those terms in the MS expansion with first scatterings at sites other than n and last scatterings at sites other than n'. This can be evaluated by substituting the representation of Eq. (A7) into Eq. (A12) and then re-expressing the terms in the site-angular momentum basis. Then $\bar{G}_{nn'}$ can be expressed in terms of the dimensionless full multiple scattering matrix elements $\bar{G}_{Ln,L'n'}$ where

$$\bar{G}(\vec{r},\vec{r}',E) = \sum_{L,L'} j_L(\vec{r}_n) \bar{G}_{Ln,L'n'} \bar{j}_L(\vec{r}_{n'})$$

$$\bar{G}_{Ln,L'n'} = [1 - \bar{G}^0 T]^{-1} \bar{G}^0|_{Ln,L'n'} \tag{A13}$$

where $\bar{G}^0_{Ln,L'n'} = G^0_{Ln,L'n'}(1-\delta_{nn'})$. The complementary delta-function in $\bar{G}^0$ ensures that $\bar{G}$ only includes initial scatterings from sites other than n and final scatterings from sites other than n'. Next the terms on the left and the right sides of Eq. (A12) can be expressed in terms of scattering states $R_{Ln}(\vec{r}_n)$. To see this note that matrix elements of the dimensionless t-matrices can be expressed in terms of phase shifts as

$$\langle j_L | \tilde{t}_n | j_{L'} \rangle = \tilde{t}_{ln} \delta_{L,L'}$$

$$\tilde{t}_{ln} = e^{i\delta_{ln}} \sin \delta_{ln}. \tag{A14}$$

Then using the representation of G^0 in terms of Bessel functions in Eq. (A6), one obtains

$$\langle \vec{r} | [1 + \tilde{G}^0 \tilde{t}_n] | LR \rangle \equiv R_{Ln}(\vec{r}_n) e^{i\delta_{ln}} = i^l [j_l(r_n) + h^+_l(r_n) \tilde{t}_{ln}] Y_L(\hat{r}_n), (r_n > r^{\mathrm{mt}}_n), \tag{A15}$$

where $R_L(\vec{r}) = i^l R_{ln}(r) Y_L(\hat{r})$. Asymptotically $R_{ln}(r) = [h^+_l e^{i\delta_{ln}} - h^-_l e^{-i\delta_{ln}}]/2i \rightarrow \sin(kr - l\pi/2 + \delta_{ln})/kr$. For $r < r^{\mathrm{mt}}$, the radial states can be obtained from the regular solution to the radial equation, matched to the above result. Similarly one obtains $\langle LR | (1 + t_n G^0) | \vec{r} \rangle = \bar{R}_L(\vec{r}_n) \exp(i\delta_{ln})$. Note that the radial functions $R_{ln}(r)$ in the scattering states are real for real non-negative k, but are otherwise the analytic continuation to complex k. Combining all these results in Eq. (A12) then yields

$$G(\vec{r},\vec{r}',E) = -2k \times \sum_{LL'} R_{Ln}(\vec{r}_n) \tilde{G}_{Ln,L'n'} \bar{R}_{L'n'}(\vec{r}_{n'}),$$

$$\tilde{G}_{Ln,L'n'} = e^{i\delta_{ln}} \bar{G}_{Ln,L'n'} e^{i\delta_{l'n'}}. \tag{A16}$$

It is straightforward to show that this expression is equivalent to that of Faulkner and Stocks.[55]

For $\vec{r}$ and $\vec{r}'$ at the same site n, $G = G^0 + G^0 t_n G^0 + \bar{G}_{n,n}$, where $\bar{G}$ is given by Eq. (A13). This yields

$$G(\vec{r},\vec{r}',E) = -2k \left[\sum_L H_{Ln}(\vec{r}_>) \bar{R}_L(\vec{r}_<) + \sum_{L,L'} R_{Ln}(\vec{r}_n) \tilde{G}_{Ln,L'n} \bar{R}_{L'n}(\vec{r}_n) \right], \tag{A17}$$

where $H_L(\vec{r})$ is the outgoing scattering state at site R which matches to $i^l e^{i\delta_{ln}} h^+_l(kr_n)$ for $r_n > r^{\mathrm{mt}}_n$.

[1] G. Onida, L. Reining, and A. Rubio, Rev. Mod. Phys. **74**, 601 (2002).
[2] P. Nozières and D. Pines, Phys. Rev. **109**, 741 (1958).
[3] H. Ehrenreich and M. H. Cohen, Phys. Rev. **115**, 786 (1959).
[4] S. L. Adler, Phys. Rev. **126**, 413 (1962).
[5] N. Wiser, Phys. Rev. **129**, 62 (1963).
[6] E. D. Palik, *Handbook of Optical Constants of Solids* (Academic Press, Orlando, 1985).
[7] W. T. Elam, B. D. Ravel, and J. R. Sieber, Radiat. Phys. Chem. **63**, 121 (2002).
[8] B. L. Henke, E. M. Gullikson, and J. C. Davis, At. Data Nucl. Data Tables **54**, 181 (1993).
[9] J. J. Yeh and I. Lindau, At. Data Nucl. Data Tables **32**, 1 (1985).
[10] H. Hagemann, W. Gudat, and C. Kunz, *Tech. Rep* (DESY, Ham-

burg, 1974).
[11] H. Hagemann, W. Gudat, and C. Kunz, J. Opt. Soc. Am. **65**, 742 (1975).
[12] A. Zangwill and P. Soven, Phys. Rev. A **21**, 1561 (1980).
[13] E. Runge and E. K. U. Gross, Phys. Rev. Lett. **52**, 997 (1984).
[14] L. J. Sham and W. Kohn, Phys. Rev. **145**, 561 (1966).
[15] G. Strinati, Phys. Rev. B **29**, 5718 (1984).
[16] M. Rohlfing and S. G. Louie, Phys. Rev. B **62**, 4927 (2000).
[17] F. Sottile, K. Karlsson, L. Reining, and F. Aryasetiawan, Phys. Rev. B **68**, 205112 (2003).
[18] P. Puschnig and C. Ambrosch-Draxl, Phys. Rev. B **66**, 165105 (2002).
[19] W. G. Schmidt, S. Glutsch, P. H. Hahn, and F. Bechstedt, Phys. Rev. B **67**, 085307 (2003).
[20] A. Marini, C. Hogan, M. Grüning, and D. Varsano, Comput. Phys. Commun. **180**, 1392 (2009).
[21] H. M. Lawler, J. J. Rehr, F. Vila, S. D. Dalosto, E. L. Shirley, and Z. H. Levine, Phys. Rev. B **78**, 205108 (2008).
[22] A. Sitt, L. Kronik, S. Ismail-Beigi, and J. R. Chelikowsky, Phys. Rev. A **76**, 054501 (2007).
[23] Y. Takimoto, F. D. Vila, and J. J. Rehr, J. Chem. Phys. **127**, 154114 (2007).
[24] J. J. Rehr and R. C. Albers, Rev. Mod. Phys. **72**, 621 (2000).
[25] G. Rivas, Ph.D. thesis, University of Washington (2004).
[26] J. D. Jackson, *Classical Electrodynamics*, 2nd ed. (John Wiley & Sons, Inc., New York, 1975).
[27] L. Reining, V. Olevano, A. Rubio, and G. Onida, Phys. Rev. Lett. **88**, 066404 (2002).
[28] I. Vasiliev, S. Öğüt, and J. R. Chelikowsky, Phys. Rev. Lett. **82**, 1919 (1999).
[29] A. V. Poiarkova and J. J. Rehr, Phys. Rev. B **59**, 948 (1999).
[30] I. P. Grant, Adv. Phys. **19**, 747 (1970).
[31] L. Hedin and S. Lundqvist, Adv. Solid State Phys., **23**, 1 (1969).
[32] J. J. Kas, A. P. Sorini, M. P. Prange, L. W. Cambell, J. A. Soininen, and J. J. Rehr, Phys. Rev. B **76**, 195116 (2007).
[33] A. L. Ankudinov and J. J. Rehr, Phys. Rev. B **56**, R1712 (1997).
[34] A. L. Ankudinov and J. J. Rehr, Phys. Rev. B **62**, 2437 (2000).
[35] E. Tamura, Phys. Rev. B **45**, 3271 (1992).
[36] A. L. Ankudinov, B. Ravel, J. J. Rehr, and S. D. Conradson, Phys. Rev. B **58**, 7565 (1998).
[37] A. L. Ankudinov, S. I. Zabinsky, and J. J. Rehr, Comput. Phys. Commun. **98**, 359 (1996).
[38] S. I. Zabinsky, J. J. Rehr, A. Ankudinov, R. C. Albers, and M. J. Eller, Phys. Rev. B **52**, 2995 (1995).
[39] N. K. del Grande, Physica Scripta **41**, 110 (1990).
[40] C. T. Chantler, C. Q. Tran, Z. Barnea, D. Paterson, D. J. Cookson, and D. X. Balaic, Phys. Rev. A **64**, 062506 (2001).
[41] M. P. Prange, J. J. Rehr, and G. Rivas, http://leonardo.phys.washington.edu/feff/opcons/.
[42] G. Galli, R. M. Martin, R. Car, and M. Parrinello, Phys. Rev. Lett. **62**, 555 (1989).
[43] G. Kresse and J. Furthmüller, Phys. Rev. B **54**, 11169 (1996).
[44] M. Newville (private communication).
[45] S. Waidmann, M. Knupfer, J. Fink, B. Kleinsorge, and J. Robertson, J. Appl. Phys. **89**, 3783 (2001).
[46] J. A. Soininen, A. L. Ankudinov, and J. J. Rehr, Phys. Rev. B **72**, 045136 (2005).
[47] R. H. French, H. Mullejans and D. J. Jones, J. Am. Ceram. Soc. **81**, 2549 (1998).
[48] C. Chantler, K. Olsen, R. Dragoset, J. Chang, A. Kishore, S. Kotochigova, and D. Zucker, http://physics.nist.gov/ffast.
[49] J. Stratton, *Electromagnetic Theory* (McGraw-Hill, New York, 1941).
[50] J. O. Cross, M. Newville, J. J. Rehr, L. B. Sorensen, C. E. Bouldin, G. Watson, T. Gouder, G. H. Lander, and M. I. Bell, Phys. Rev. B **58**, 11215 (1998).
[51] U. Hartmann, Phys. Rev. B **42**, 1541 (1990).
[52] A. P. Sorini, J. J. Kas, J. J. Rehr, M. P. Prange, and Z. H. Levine, Phys. Rev. B **74**, 165111 (2006).
[53] M. Altarelli, D. L. Dexter, H. M. Nussenzveig, and D. Y. Smith, Phys. Rev. B **6**, 4502 (1972).
[54] J. J. Rehr and R. C. Albers, Phys. Rev. B **41**, 8139 (1990).
[55] J. S. Faulkner and G. M. Stocks, Phys. Rev. B **21**, 3222 (1980).